Editors' Suggestion

Magnetic Domains without Domain Walls: A Unique Effect of He^+ Ion Bombardment in Ferrimagnetic Tb/Co Films

Łukasz Frąckowiak,[1] Piotr Kuświk,[1,*] Gabriel David Chaves-O'Flynn,[1] Maciej Urbaniak,[1] Michał Matczak,[2] Paweł Piotr Michałowski,[3] Andrzej Maziewski,[2] Meike Reginka,[4] Arno Ehresmann,[4] and Feliks Stobiecki[1,†]

[1]*Institute of Molecular Physics, Polish Academy of Sciences, Smoluchowskiego 17, 60-179 Poznań, Poland*
[2]*Faculty of Physics, University of Białystok, Ciołkowskiego 1L, 15-245 Białystok, Poland*
[3]*Łukasiewicz Research Network—Institute of Electronic Materials Technology, Wólczyńska 133, 01-919 Warszawa, Poland*
[4]*Institute of Physics and Center for Interdisciplinary Nanostructure Science and Technology (CINSaT), University of Kassel, Heinrich-Plett-Str. 40, 34132 Kassel, Germany*

(Received 3 August 2019; revised manuscript received 13 November 2019; published 30 January 2020)

We show that it is possible to engineer magnetic multidomain configurations without domain walls in a prototypical rare-earth–transition-metal ferrimagnet using keV He^+ ion bombardment. We additionally show that these patterns display a particularly stable magnetic configuration due to a deep minimum in the energy of the system caused by flux closure and a corresponding reduction of the magnetostatic energy without an increase in energy by exchange and anisotropy terms across the walls. This occurs because light-ion bombardment affects an element's relative contribution to the properties of the ferrimagnet differently. Therefore, it is possible to control the relative contribution from each magnetic subsystem. The selection of material and the use of light-ion bombardment allow us to engineer domain patterns in continuous magnetic films, which open a way to fabricate them in a much smaller scale than currently possible. Our Letter emphasizes that the right criterion to determine the presence or absence of a domain wall is whether there is a rotation of the spin for each sublattice and that changes of the direction of effective magnetization alone do not constitute an appropriate criterion.

DOI: 10.1103/PhysRevLett.124.047203

The ability to create lateral magnetic domain patterns in ferromagnetic films is crucial for numerous applications. Their use in magnetic mass memories [1–3] is established, but they are also useful in magnonics [4,5] and in magnetophoresis-based lab-on-a-chip devices [6–9]. In ferromagnets, magnetic domains are uniformly magnetized regions, in which the effective magnetization points in a defined direction. Naturally occurring domain patterns are formed as a result of a compromise among exchange, anisotropy, and stray field energy [4,6,10,11]. The domains are separated by domain walls (DWs), which are transition regions where the magnetic moments reorient. Their widths are the natural size limit for individual domains. Therefore, the lateral DW widths are also the critical dimension for magnetic domains in continuous layers. Domain patterns can be engineered by local modification of magnetic properties such as the coercive field (H_C) [12–15]. In the past, this has been achieved, e.g., by light-ion bombardment through masks [13,14,16,17] or by focused ion beams [18–21]. However, even these precise methods are not able to engineer domains of lateral dimensions below the corresponding DW widths.

Here we describe a method to engineer magnetic domain patterns without lateral DWs in a ferrimagnetic system. This unique method promises magnetic domains in continuous layer systems of dimensions well below the typical ferromagnetic DW widths. Although the physics of magnetic domain formation in ferrimagnetic films is similar to that in ferromagnetic films [10], the presence of two magnetic moment subsystems leads to more complex configurations. Exchange coupled double layers (ECDL) consisting of rare-earth (RE)–transition-metal (TM) elements with alternating stoichiometric domination of RE (RE+) or TM (TM+) will contain interfacial DWs at saturation and lack of them at remanence [22–28] (Fig. 1 in Ref. [24] and Fig. 1 in Ref. [28]). This peculiar situation is possible because parallel effective magnetizations (monodomain state) in the RE+ and TM+ layers correspond to antiparallel magnetic moments of the magnetic subsystems (DW is present) of the same type (RE or TM) [24] (in Ref. [28] this magnetic state is described as an interfacial DW separating two domains with the same direction of the effective magnetization). After the magnetization reverses in one of the layers, the magnetization of the layers will be oriented antiparallel to each other. However, the magnetization of each subsystem will maintain its orientation on both sides of the interface (DW is not present and that can be described as a nontwisted domain wall). It should be emphasized that in ECDL films the switching fields are distinctly influenced by creation and annihilation of interfacial DWs. Note that the first studies of ECDL consisting of RE+ and TM+ sublayers were performed on alloyed RE-TM films in which the upper part of a RE- dominated

 © 2020 American Physical Society

film was transformed into TM+ due to preferential oxidation of the RE element [29].

We will demonstrate that He^+ ion bombardment allows us to modify the magnetic properties of ferrimagnetic Tb/Co films exhibiting perpendicular magnetic anisotropy [30–36]. We will also show that, with increasing dose of He^+ ions, the Tb contribution to the effective magnetization decreases strongly relative to Co. This opens a way to pattern RE+ ferrimagnetic films with light ions to locally switch the domination to TM+. Thus, analogous to ferrimagnetic ECDL films, magnetic domains can be produced at remanence without DWs. Using this patterning technique, we have fabricated a laterally periodic domain pattern consisting of a lattice of low H_C TM+ squares embedded in a high H_C RE+ matrix.

The subjects of our investigations are Tb/Co multilayers displaying, for small sublayer thicknesses, magnetic properties similar to amorphous Tb-Co alloy films [30–34]. The $(\text{Tb-wedge0-2 nm/Co-0.66 nm})_6$ layer system was magnetron sputtered to determine the influence of the 10 keV He^+ ion bombardment on the properties of the $(\text{Tb/Co})_6$ films as a function of the thickness ratio between Co and Tb layers, i.e., as a function of the nominal composition. The sample was bombarded with two He^+ ion doses D of 1×10^{15} and 3×10^{15} ions/cm^2 using a home-built plasma source [37] (details are given in the Supplemental Material [38]). The composition depth profiles of the as-deposited and bombarded samples were investigated by secondary ion mass spectroscopy (SIMS) (Fig. 1) with the CAMECA SC Ultra instrument [39–41] (see Supplemental Material [38]). These results confirm that, before and after ion bombardment, the samples show similar and weak depth-dependent modulation of composition.

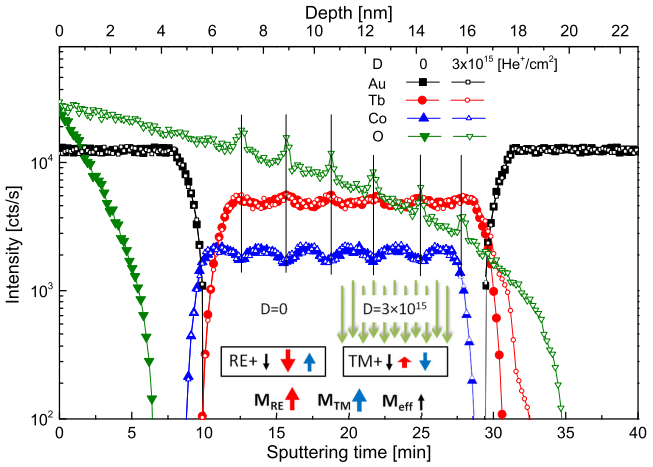

FIG. 1. SIMS depth profile of Si/Ti-4 nm/Au-30 nm/$(\text{Tb-1.1 nm/Co-0.66 nm})_6$/Au-5 nm in the as-deposited state (closed symbols) and after He^+ bombardment (open symbols) with the dose $D = 3 \times 10^{15}$ He^+/cm^2. Note that, after ion bombardment, the O signal maxima correspond to the Tb maxima and Co minima (marked as vertical lines). Inset shows the magnetic configuration at saturation before and after ion bombardment.

The magnetic properties were investigated with a magnetometer and a microscope using the polar magneto-optical Kerr effect (P-MOKE). Figure 2 shows changes of the coercive field as a function of the Tb sublayer thickness $[H_C(t_{\text{Tb}})]$ for an unbombarded area and two areas bombarded with $D = 1 \times 10^{15}$ He^+/cm^2 and $D = 3 \times 10^{15}$ He^+/cm^2. The singularities in the curves $H_C(t_{\text{Tb}}; D)$ correspond to the Tb layer thicknesses $t_{\text{Tb}}^{\text{comp}}$ and the associated effective Tb concentration $c_{\text{Tb}}^{\text{comp}}$ at which the magnetic moments of Co and Tb compensate each other [Fig. 2(a)]. Note that the hysteresis loops for systems with Tb and Co domination have opposite orientations [Figs. 2(b)–2(d)]. This occurs because, for the wavelength used in the P-MOKE setup (640 nm), the Co subsystem determines the sign of the magneto-optical signal [30,42,43].

It can be seen that the $t_{\text{Tb}}^{\text{comp}}$ and $c_{\text{Tb}}^{\text{comp}}$ values increase with increasing D, showing that the relative magnetic contribution of Tb to ferrimagnetic properties of the Tb/Co system can be reduced by ion bombardment. Let us analyze the changes of the magnetic properties of the Tb/Co system with $t_{\text{Tb}} = 1.1$ nm ($t_{\text{Tb}} > t_{\text{Tb}}^{\text{comp}}$) caused by ion bombardment. In the as-deposited state, this system is Tb+ [Fig. 2(b)]. After ion bombardment with $D = 1 \times 10^{15}$ He^+/cm^2 [Fig. 2(c)], the hysteresis loop still has an orientation indicating the same dominance, but now H_C

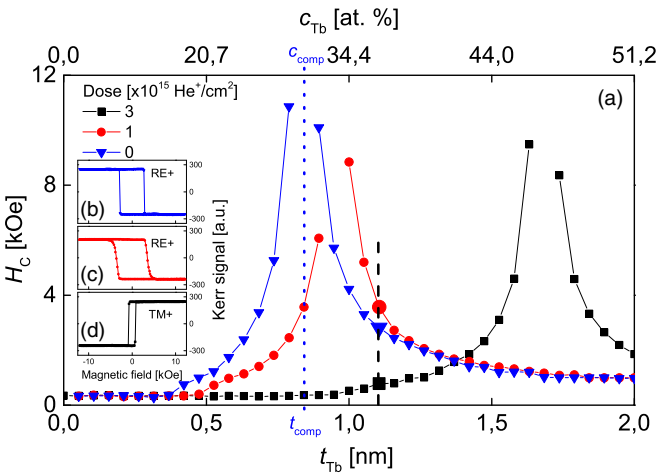

FIG. 2. (a) Coercive field H_C as a function of the Tb sublayer thicknesses of the Si/Ti-4 nm/Au-30 nm/$(\text{Tb-wedge/Co-0.66 nm})_6$/Au system in the as-deposited state and after He^+ (10 keV) ion bombardment with dose $D = 1 \times 10^{15}$ He^+/cm^2 and $D = 3 \times 10^{15}$ He^+/cm^2. The upper horizontal axis shows the corresponding effective concentration of Tb (c_{Tb}) for a given Tb thickness. The dashed line corresponds to $t_{\text{Tb}} = 1.1$ nm, which was chosen for the experiments presented in this figure. The hysteresis loops corresponding to large points ($t_{\text{Tb}} = 1.1$ nm) in panel (a) are presented in panels (b), (c), and (d) for $D = 0$, $D = 1 \times 10^{15}$ He^+/cm^2, and $D = 3 \times 10^{15}$ He^+/cm^2, respectively.

is higher. Increasing D to 3×10^{15} He^+/cm^2 [Fig. 2(d)] modifies the system so that the Co magnetic subsystem starts to dominate.

The change of the SIMS depth profile caused by bombardment with $D = 3 \times 10^{15}$ He^+/cm^2, $(Tb\text{-}1.1\ nm/Co\text{-}0.66\ nm)_6$ (Fig. 1) strongly suggests that a decrease of the Tb contribution to the ferrimagnetic properties of the Tb/Co system is mainly caused by the preferential oxidation of Tb. In particular, this is confirmed by the concurrence of terbium and oxygen peaks in the depth profile of the bombarded sample. The results presented in Figs. 1 and 2 indicate that, by using local ion bombardment for the Tb-dominated Tb/Co system, heterostructures consisting of Co-dominating areas can be created in a Tb-dominated matrix. By analogy with the system described in Ref. [24], this is an important result, paving the way for engineering magnetic patterns without DWs.

To prove such a possibility, we performed He^+ ion bombardment through a resist mask with dose $D = 3 \times 10^{15}$ He^+/cm^2 (see Supplemental Material [38]) for a selected $t_{Tb} = 1.1$ nm and studied the magnetization reversal of the magnetically patterned $(Tb\text{-}1.1\ nm/Co\text{-}0.66\ nm)_6$ film. Note that the bombarded areas are TM+, in contrast to the matrix, and have lower H_C. Four 1×1 mm^2 areas were patterned on the same sample with periodically arranged squares of side lengths $a = 3$, 12.5, 25, and 100 μm and distances between the centers of neighboring squares of $2a$ (see Fig. S1 in the Supplemental Material [38]).

Full and minor P-MOKE hysteresis loops for all patterned areas are shown in Fig. 3(a), and the magnetic moment configurations of the two magnetic subsystems of the ferrimagnet corresponding to the states 1–4 in the loops are sketched in Fig. 3(c). The Co and Tb spin distributions at the interface between RE+ and TM+ areas in states 1 and 2 are shown in Figs. 4(e) and 4(g), respectively. Additionally, reference MOKE measurements were performed on a 1×1 mm^2 area bombarded with $D = 3 \times 10^{15}$ He^+/cm^2, as well as for an unbombarded area [Fig. 3(b)]. Note that the dimensions of the reference areas were much larger than the laser spot used for the P-MOKE characterization. Therefore, the hysteresis loops measured in the central part of the reference areas are not affected by the border regions between the bombarded and unbombarded areas. The situation is different for the patterned periodic square lattices where hysteresis loops are the approximate superposition of those obtained for the reference areas. The P-MOKE signal ratio corresponding to magnetization reversal of the squares and matrix is equal to the ratio of the areas of these regions, which is 1/3. Only for the largest squares the observed ratio is not exactly 1/3 because the size of the individual squares approaches the diameter of the P-MOKE laser spot; in consequence, the signal does not average over several squares.

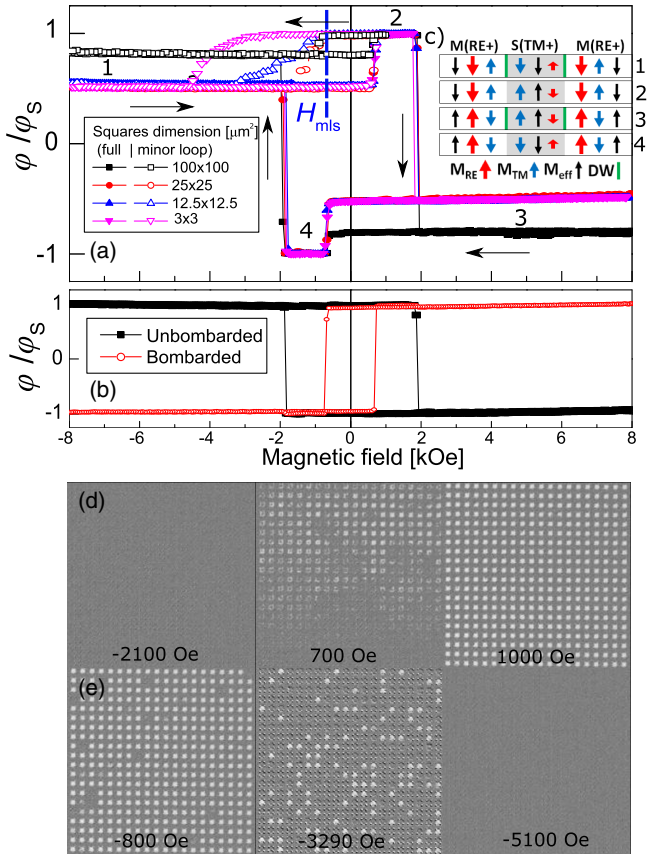

FIG. 3. Full and minor (full and open symbols, respectively) P-MOKE hysteresis loops measured for a Si/Ti-4 nm/Au−30 nm/(Tb−1.1 nm/Co−0.66 nm)$_6$/Au−5 nm system magnetically patterned using ion bombardment (He^+ 10 keV) with dose $D = 3 \times 10^{15}$ He^+/cm^2 (a),(b). The different colors in panel (a) correspond to different sizes of patterned squares (pink, 3×3 μm^2; blue, 12.5×12.5 μm^2; red, 25×25 μm^2; black, 100×100 μm^2). The hysteresis loops presented in panel (b) correspond to references of bombarded (red) and unbombarded (black) areas. The magnetic field corresponding to the minor loop shift H_{MLS} is indicated only for $a = 12.5$ μm. Panel (c) shows the magnetization orientation in the matrix (M) and the squares (S). The black, blue, and red arrows correspond to effective magnetization, magnetization of the Co, and of the Tb magnetic subsystems, respectively. DWs are indicated with green. Panels (d),(e) show differential images (difference between images recorded at a given magnetic field and at saturation in negative field) of the magnetic structure recorded using P-MOKE. The photographs present only ¼ of the full lattice and are arranged in rows corresponding to magnetic field ranges related to the minor loop reversal of the 12.5×12.5 μm^2 squares from 1 to 2 (d) and from 2 to 1 (e).

Hereinafter, the switching fields H_S^{if} will identify transitions between the specific states marked with superscripts for the initial (i) and final (f) states; e.g., H_S^{12} and H_S^{34} correspond to the magnetization reversal of squares. A weak dependence of the switching fields (H_S) on the square side a is observed for H_S^{23} and H_S^{41}, whereas essentially no dependence is observed for H_S^{34} and H_S^{12} [Fig. 3(a)].

This indicates a relatively weak magnetostatic interaction between the squares and matrix due to the low saturation magnetization (M_S) and small thicknesses of the films [44]. Exchange coupling at the borders between the squares and matrix contributes weakly, too, to the effective interaction because of the small interaction surface (film thickness multiplied by the perimeter length of a square).

Since the bombarded areas have lower H_S and are TM+ and the matrix is RE+ with higher H_S, then the magnetization reversals $1 \rightarrow 2$ and $3 \rightarrow 4$ occur inside the squares (Fig. 2S and Video 1 in the Supplemental Material [38]). In states 1 and 3 (at saturation), the effective magnetizations of the squares and matrix are both oriented along the magnetic field; at the same time, the magnetizations of each magnetic subsystem (Co and Tb) rotate to the antiparallel direction across the borders between the squares and matrix [Figs. 3(c) and 4(e)]. Therefore, in states 1 and 3, DWs exist at the borders of the squares. At fields H_S^{12} and H_S^{34}, the squares reverse (the effective magnetizations of the squares and matrix are now antiparallel to each other) and the DWs are annihilated.

The comparison of the magnetic configurations of states 1(3) and 2(4) [Figs. 3(a) and 3(c)] suggest that, at remanence, states 2 and 4 are energetically more favorable than states 1 and 3. This is caused by both a reduction of the magnetostatic energy (the effective magnetization in the squares is antiparallel to that of the matrix) and by the annihilation of DWs (note that, in contrast to the situation of ECDL films [24], the same orientation of effective magnetizations increases the magnetostatic energy). As a result, processes $1 \rightarrow 2$ and $3 \rightarrow 4$ involve a reduction of the free energy in the system, while the opposite processes ($2 \rightarrow 1$ and $4 \rightarrow 3$, in minor loops) are accompanied by an increase. Although the individual squares reverse independently, the values H_S^{12} and H_S^{34} [Fig. 3(a)] are close to the H_C value of the modified reference area [Fig. 3(b)] and show a narrow distribution, while $|H_S^{21}|$ and $|H_S^{43}|$ ($4 \rightarrow 3$, not shown) are greater than the $|H_C|$ of the reference area and have a large spread [Fig. 3(d)] (see Video 2 in the Supplemental Material [38]). The influence of a on the abovementioned switching fields is stronger for smaller a (the greater sum of DW lengths), and their increased spread broadening as a is reduced can be attributed to the spatial distribution of magnetic properties due to deposition and ion bombardment through the resist [45–47]. For the magnetic file sweep direction used in our experiment, the shift of minor loops (H_{MLS}) seen in Fig. 3(a) is negative, indicating an antiferromagnetic coupling between the TM+ squares and the RE+ matrix. The origin of this coupling is related to the elimination of the antiparallel configuration of magnetization in the Co and Tb magnetic subsystems (annihilation of DWs). Processes $2 \rightarrow 3$ and $4 \rightarrow 1$ take place by propagation of DWs in the matrix (see Fig. 3S in the Supplemental Material [38]) and involve DW creation.

To support qualitatively our interpretation of the experimental data, we have performed micromagnetic simulations using the object oriented micromagnetic framework (OOMMF) [48] without any additional extensions. Details are described in the Supplemental Material [38], but the essentials can be described as follows: We generate a grid of cubic cells of side 0.5 nm and randomly assign a magnetic material (RE or TM) to each cell to mimic their corresponding concentrations (65% TM, 35% RE). In the bombarded area, we deactivate a fraction of the cells assigned to the rare-earth element (71%) by reducing their magnetization to zero to model its oxidation.

Typical full and minor simulated loops for the patterned strip are shown in Fig. 4(a). The full loop is a two-step hysteresis with intermediate states similar to those described in the discussion of Fig. 3(a). Note that in Fig. 3(a), the dependence of the P-MOKE signal (strongly dominated by the Co subsystem) on the magnetic field is shown, while in Fig. 4(a), the one of the effective magnetization is shown. State 1 corresponds to saturation in negative field where the effective moments in both RE+ and TM+ regions are aligned parallel to the field [Fig. 4(f)]; for state 2, the effective moment in the bombarded area is opposite that of the matrix [Fig. 4(h)]. Close-up views of these configurations are shown in Figs. 4(e)) and 4(g). These transversal cross sections show the difference between the two states: In state 1, the effective magnetization is negative everywhere, except precisely at the edge of the bombarded area where the magnetization of each subsystem undergoes rotation, i.e., where the DWs are located; while state 2 does not contain a DW even though the two regions have opposite effective magnetizations. These two images support the key finding of our Letter, namely, that a RE+ ferrimagnetic system can be patterned by keV He ion bombardment allowing multiple domains without DWs (states 2, 4). Because of the strong antiferromagnetic coupling between the Co and the Tb subsystems [49], the spin structure of the DWs is similar to the interfacial DWs found in the ECDL films (Fig. 14 in Ref. [50]).

Having shown that in ferrimagnetic films consisting of TM+ areas embedded in an RE+ matrix the antiparallel configuration of the effective magnetization can exist without DWs at the borders between the RE+ and TM+ areas, we now show that at the field-induced transition between states 1 and 2, the reduction in anisotropy energy and exchange energy is accompanied by a reduction of magnetostatic energy. Overall, flux closure is achieved with the annihilation of the DW. Figures 4(b)–4(d) show the anisotropy, magnetostatic, and exchange energies as a function of the magnetic field for the down sweep branch of the hysteresis loop. In state 2, which occupies the middle region of this graph (-1.9 kOe $\leq H \leq -0.3$ kOe), we see that due to annihilation of DWs the exchange energy and the sum of the anisotropy and magnetostatic energies are reduced. It is also apparent that the magnetostatic energy in state 2 is generally lower than in state 1. Therefore, such a

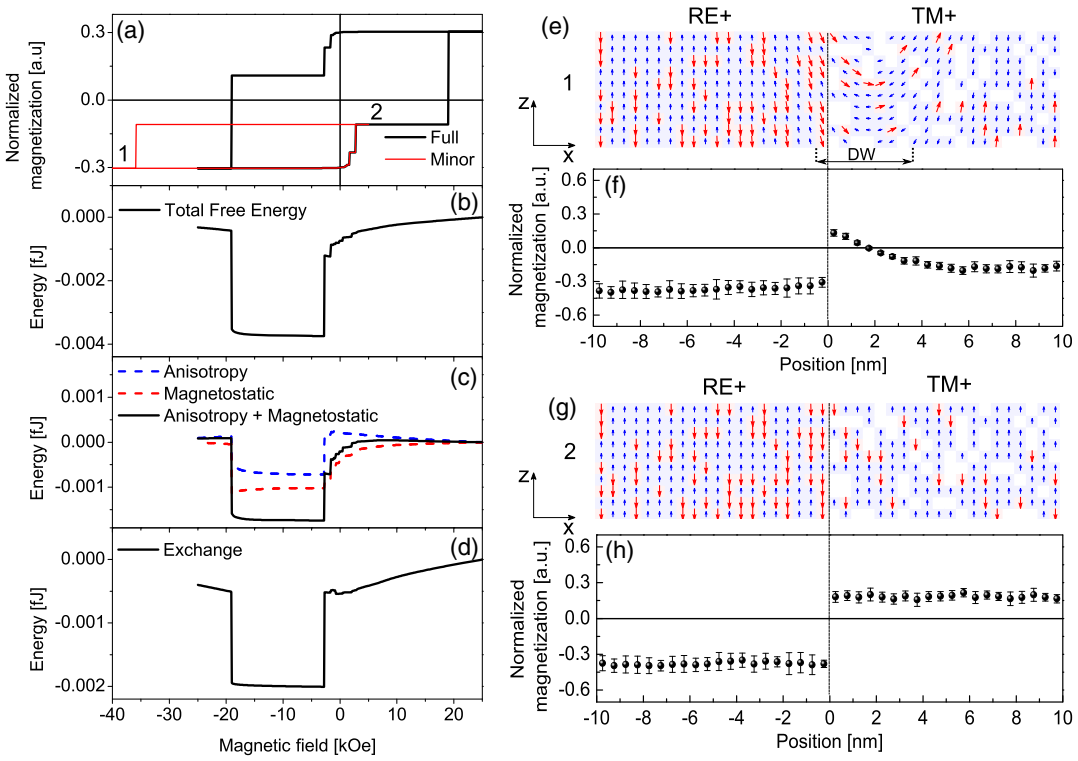

FIG. 4. (a) Full and minor hysteresis loops obtained from OOMMF simulations for a patterned strip for randomized distributions of Tb cells. The magnetization perpendicular to the plane m_z is normalized accounting for the total number of Co and Tb cells. (b) Free energy (magnetostatic + anisotropy + exchange), (c) sum of anisotropy and magnetostatic energies, and (d) exchange energy as functions of the applied field for the sweep of the hysteresis loop from 25 to −25kOe. To facilitate comparison, the energy terms in the saturated state are set to zero. (e),(g) Cross section of the Co (blue arrows) and Tb (red arrows) magnetization configuration in the region between the RE+ and TM+ areas at magnetic field $H = 25$ kOe and $H = -3$ kOe corresponding to states 1 and 2. In the bombarded area, a fraction of rare-earth atoms are deactivated to model their oxidation (white cells). (f),(h) Normalized m_z component at distance x away from the boundary between the RE+ and the TM+ regions. The error bars in (f) and (h) correspond to the standard deviation of ten simulations with different random distributions.

magnetic configuration is very stable and is characterized by a deep free-energy minimum, which explains the strong negative value of H_{MLS} observed both in experiment [Fig. 3(a)] and simulations [Fig. 4(a)]. This confirms that it is possible to achieve flux closure in the absence of DWs, which explains why the observed unique features are particularly stable and energetically advantageous.

It has been shown that, in a rare-earth–transition-metal ferrimagnetic system, magnetic domains can be engineered without DWs using 10 keV He^+ ion bombardment. These magnetic configurations are particularly stable due to a deep minimum in the free energy of the system, which is caused by flux closure and the corresponding reduction of magnetostatic energy without an increase in energy by exchange and anisotropy terms across the walls. As a result, a much larger magnetic field is required to annihilate such a magnetic pattern than to create it. The fundamental effect used for engineering of such domains without DWs is that the impact of keV light-ion bombardment to effective properties of ferrimagnetic films is related to preferential oxidation of rare earth. Therefore, the technique can be used in this system to control the relative contributions of the two magnetic subsystems. Thus, starting with magnetic Tb/Co films where the Tb magnetization dominates and using ion bombardment, we have created magnetic patterns where areas with Co magnetic moment density domination and small coercive fields were embedded in the matrix that retained the magnetic properties of the as-deposited system.

The authors would like to thank M. Schmidt and J. Aleksiejew for technical support. The work was financed by the National Science Centre Poland under SONATA BIS funding Grant No. UMO-2015/18/E/ST3/00557. M. M. and A. M. acknowledge financial support from the National Science Centre Poland through the SONATINA Project No. UMO-2018/28/C/ST5/00308. F. S. acknowledge support from the National Science Centre Poland through the PRELUDIUM Project No. UMO-2018/31/N/ST5/01810.

*Corresponding author.
kuswik@ifmpan.poznan.pl
†Corresponding author.
feliks.stobiecki@ifmpan.poznan.pl

[1] A. Moser, K. Takano, D. T. Margulies, M. Albrecht, Y. Sonobe, Y. Ikeda, S. Sun, and E. E. Fullerton, Magnetic recording: Advancing into the future, J. Phys. D **35**, R157 (2002).

[2] J. I. Martin, J. Nogues, K. Liu, J. L. Vincent, and I. K. Schuller, Ordered magnetic nanostructures: Fabrication and properties, J. Magn. Magn. Mater. **256**, 449 (2003).

[3] B. D. Terris, T. Thomson, and G. Hu, Patterned media for future magnetic data storage, Microsyst. Technol. **13**, 189 (2006).

[4] L. Fallarino, A. Oelschlägel, J. A. Arregi, A. Bashkatov, F. Samad, B. Böhm, K. Chesnel, and O. Hellwig, Control of domain structure and magnetization reversal in thick Co/Pt multilayers, Phys. Rev. B **99**, 024431 (2019).

[5] F. Ando, M. Ishibashi, T. Koyama, Y. Shiota, T. Moriyama, D. Chiba, and T. Ono, Magnetic domain writing defined by electrical gating in Pt/Co film, Appl. Phys. Lett. **113**, 252402 (2018).

[6] P. Tierno, T. H. Johansen, and T. M. Fischer, Magnetically driven colloidal microstirrer, J. Phys. Chem. B **111**, 3077 (2007).

[7] J. Loehr *et al.* Lattice symmetries and the topologically protected transport of colloidal particles, Soft Matter **13**, 5044 (2017).

[8] J. Loehr *et al.*, Colloidal topological insulators, Commun. Phys. **1**, 4 (2018).

[9] D. Holzinger, I. Koch, S. Burgard, and A. Ehresmann, Directed magnetic particle transport above artificial magnetic domains due to dynamic magnetic potential energy landscape transformation, ACS Nano **9**, 7323 (2015).

[10] A. Hubert and R. Schäfer, *Magnetic Domains: The Analysis of Magnetic Microstructures* (Springer, New York, 1998).

[11] M. Hehn, S. Padovani, K. Ounadjela, and J. P. Bucher, Nanoscale magnetic domain structures in epitaxial cobalt films, Phys. Rev. B **54**, 3428 (1996).

[12] J.-P. Adam, J.-P. Jamet, J. Ferré, A. Mougin, S. Rohart, R. Weil, E. Bourhis, and J. Gierak, Magnetization reversal in Pt/Co(0.5 nm)/Pt nano-platelets patterned by focused ion beam lithography, Nanotechnology **21**, 445302 (2010).

[13] P. Kuświk, I. Sveklo, B. Szymański, M. Urbaniak, F. Stobiecki, A. Ehresmann, D. Engel, P. Mazalski, A. Maziewski, and J. Jagielski Colloidal domain lithography in multilayers with perpendicular anisotropy: An experimental study and micromagnetic simulations, Nanotechnology **23**, 475303 (2012).

[14] P. Kuświk *et al.*, Colloidal domain lithography for regularly arranged artificial magnetic out-of-plane monodomains in Au/Co/Au layers, Nanotechnology **22**, 095302 (2011).

[15] C. Chappert, Planar patterned magnetic media obtained by ion irradiation, Science **280**, 1919 (1998).

[16] A. Ehresmann, I. Koch, and D. Holzinger, Manipulation of superparamagnetic beads on patterned exchange-bias layer systems for biosensing applications, Sensors **15**, 28854 (2015).

[17] A. Ehresmann, D. Lengemann, T. Weis, A. Albrecht, J. Langfahl-Klabes, F. Göllner, and D. Engel, Asymmetric magnetization reversal of stripe-patterned exchange bias layer systems for controlled magnetic particle transport, Adv. Mater. **23**, 5568 (2011).

[18] P. Warin, R. Hyndman, J. Glerak, J. N. Chapman, J. Ferré, J. P. Jamet, V. Mathet, and C. Chappert, Modification of Co/Pt multilayers by gallium irradiation—Part 2: The effect of patterning using a highly focused ion beam, J. Appl. Phys. **90**, 3850 (2001).

[19] J. Gierak *et al.* Exploration of the ultimate patterning potential achievable with focused ion beams, Microelectron. Eng. **78–79**, 266 (2005).

[20] A. Gaul *et al.* Size limits of magnetic-domain engineering in continuous in-plane exchange-bias prototype films, Beilstein J. Nanotechnol. **9**, 2968 (2018).

[21] P. Mazalski, P. Kuświk, I. Sveklo, I. Soldatov, J. McCord, R. Schäfer, A. Wawro, and A. Maziewski, Modification of magnetization ordering in Pt/Co/Pt trilayers depending on the scanning direction of a focused ion beam, J. Magn. Magn. Mater. **477**, 317 (2019).

[22] C. Blanco-Roldán, Y. Choi, C. Quirós, S. M. Valvidares, R. Zarate, M. Vélez, J. M. Alameda, D. Haskel, and J. I. Martín, Tuning interfacial domain walls in GdCo/Gd/GdCo′ spring magnets, Phys. Rev. B **92**, 224433 (2015).

[23] B. Hebler, P. Reinhardt, G. L. Katona, O. Hellwig, and M. Albrecht, Double exchange bias in ferrimagnetic heterostructures, Phys. Rev. B **95**, 104410 (2017).

[24] T. Kobayashi, H. Tsuji, S. Tsunashima, and S. Uchiyama, Magnetization process of exchange-coupled ferrimagnetic double-layered films, Jpn. J. Appl. Phys. **20**, 2089 (1981).

[25] F. Stobiecki, T. M. Atmono, S. Becker, H. Rohrmann, and K. Röll, Investigation of interface wall energy σw and coercivity HC in exchange-coupled double layers (ECDLs), J. Magn. Magn. Mater. **148**, 497 (1995).

[26] K. Wang, Y. Wang, F. Ling, and Z. Xu, Perpendicular exchange coupling effects in ferrimagnetic TbFeCo/GdFeCo hard/soft structures, J. Magn. Magn. Mater. **452**, 153 (2018).

[27] T. Hauet, F. Montaigne, M. Hehn, Y. Henry, and S. Mangin, Magnetoresistance in an amorphous exchange-coupled bilayer, Phys. Rev. B **79**, 224435 (2009).

[28] P. Hansen, New type of compensation wall in ferrimagnetic double layers, Appl. Phys. Lett. **55**, 200 (1989).

[29] B. E. Argyle, R. J. Gambino, and K. Y. Ahn, Polar Kerr rotation and sublattice magnetization in GdCoMo bubble films, AIP Conf. Proc. **24**, 564 (1975).

[30] Ł. Frąckowiak, P. Kuświk, M. Urbaniak, G. D. Chaves-O'Flynn, and F. Stobiecki, Wide-range tuning of interfacial exchange coupling between ferromagnetic Au/Co, and ferrimagnetic Tb/Fe(Co) multilayers, Sci. Rep. **8**, 16911 (2018).

[31] L. Ertl, G. Endl, and H. Hoffmann, Structure and magnetic properties of sputtered Tb/Co multilayers, J. Magn. Magn. Mater. **113**, 227 (1992).

[32] J. Šmakov, S. Lapinskas, E. E. Tornau, and A. Rosengren, Magnetization and compensation temperature of transition-metal–rare-earth multilayers in a model with long-range interactions, J. Magn. Magn. Mater. **190**, 157 (1998).

[33] G. Garreau, M. Farle, E. Beaurepaire, and J. P. Kappler, Spin-reorientation phase transition in Co/Tb and Co/Ho ultrathin films, J. Magn. Magn. Mater. **184**, 289 (1998).

[34] A. V. Svalov, P. A. Savin, G. V. Kurlyandskaya, J. Gutiérrez, and V. O. Vas'kovskiy, Spin-valve magnetoresistive structures based on Co/Tb multilayer films, Tech. Phys. **47**, 987 (2002).

[35] M. H. Tang, Z. Zhang, S. Y. Tian, J. Wang, B. Ma, and Q. Y. Jin, Interfacial exchange coupling and magnetization reversal in perpendicular [Co/Ni]N/TbCo composite structures, Sci. Rep. **5**, 10863 (2015).

[36] C. Schubert, *Magnetic Order and Coupling Phenomena* (Springer International Publishing, New York, 2014).

[37] D. Lengemann, D. Engel, and A. Ehresmann, Plasma ion source for in situ ion bombardment in a soft x-ray magnetic scattering diffractometer, Rev. Sci. Instrum. **83**, 053303 (2012).

[38] See Supplemental Material at http://link.aps.org/supplemental/10.1103/PhysRevLett.124.047203 for detailed description of sample deposition, ion bombardment, secondary mass spectroscopy measurements, magnetic properties characterization, micromagnetic simulations and magnetization reversal process.

[39] P. P. Michałowski, W. Kaszub, A. Merkulov, and W. Strupiński, Secondary ion mass spectroscopy depth profiling of hydrogen-intercalated graphene on SiC, Appl. Phys. Lett. **109**, 011904 (2016).

[40] P. P. Michałowski, P. Gutowski, D. Pierścińska, K. Pierściński, M. Bugajski, and W. Strupiński Characterization of the superlattice region of a quantum cascade laser by secondary ion mass spectrometry, Nanoscale **9**, 17571 (2017).

[41] P. P. Michałowski, E. Grzanka, S. Grzanka, A. Lachowski, G. Staszczak, J. Plesiewicz, M. Leszczyński, and A. Turos Indium concentration fluctuations in InGaN/GaN quantum wells, J. Anal. At. Spectrom. **34**, 1718 (2019).

[42] S. Alebrand, U. Bierbrauer, M. Hehn, M. Gottwald, O. Schmitt, D. Steil, E. E. Fullerton, S. Mangin, M. Cinchetti, and M. Aeschlimann Subpicosecond magnetization dynamics in TbCo alloys, Phys. Rev. B **89**, 144404 (2014).

[43] A. Hassdenteufel, C. Schubert, J. Schmidt, P. Richter, D. R. T. Zahn, G. Salvan, M. Helm, R. Bratschitsch, and M. Albrecht Dependence of all-optical magnetic switching on the sublattice magnetization orientation in Tb-Fe thin films, Appl. Phys. Lett. **105**, 112403 (2014).

[44] J. Norpoth, S. Dreyer, and C. Jooss, Straightforward field calculations for uniaxial hard magnetic prisms: Stray field distributions and dipolar coupling in regular arrays, J. Phys. D **41**, 025001 (2008).

[45] J.-P. Jamet *et al.*, Dynamics of the magnetization reversal in Au/Co/Au micrometer-size dot arrays, Phys. Rev. B **57**, 14320 (1998).

[46] M. Kisielewski, J. Kisielewski, I. Sveklo, A. Wawro, and A. Maziewski, Micromagnetic simulations of magnetization spatial distribution in ultrathin cobalt layers with gradient magnetic anisotropy, IEEE Trans. Magn. **53**, 1 (2017).

[47] T. Devolder, Light ion irradiation of Co/Pt systems: Structural origin of the decrease in magnetic anisotropy, Phys. Rev. B **62**, 5794 (2000).

[48] M. Donahue and D. G. Porter, OOMMF User's Guide, Version 1.0 (National Institute of Standards and Technology, Gaithersburg, MD, 1999) [http://math.nist.gov/oommf].

[49] N. H. Duc, T. D. Hien, D. Givord, J. J. M. Franse, and F. R. de Boer, Exchange interactions in rare earth–transition metal compounds, J. Magn. Magn. Mater. **124**, 305 (1993).

[50] S. Tsunashima, Magneto-optical recording, J. Phys. D **34**, R87 (2001).